

See discussions, stats, and author profiles for this publication at: <https://www.researchgate.net/publication/251590231>

Visualizing photovoltaic nanostructures with high-resolution analytical electron microscopy reveals material phases in bulk heterojunctions

ARTICLE in SYNTHETIC METALS · JANUARY 2012

Impact Factor: 2.25 · DOI: 10.1016/j.synthmet.2011.09.011

CITATIONS

8

READS

68

6 AUTHORS, INCLUDING:



Martin Pfannmöller
University of Antwerp
13 PUBLICATIONS 151 CITATIONS

[SEE PROFILE](#)



Gerd Benner
Carl Zeiss AG
71 PUBLICATIONS 802 CITATIONS

[SEE PROFILE](#)



Irene Wacker
Universität Heidelberg
28 PUBLICATIONS 1,017 CITATIONS

[SEE PROFILE](#)

Visualizing a Homogeneous Blend in Bulk Heterojunction Polymer Solar Cells by Analytical Electron Microscopy

Martin Pfannmöller,^{*,†} Harald Flügge,[‡] Gerd Benner,[§] Irene Wacker,^{||} Christoph Sommer,[⊥] Michael Hanselmann,[⊥] Stephan Schmale,[‡] Hans Schmidt,[‡] Fred A. Hamprecht,[⊥] Torsten Rabe,[‡] Wolfgang Kowalsky,^{*,#} and Rasmus R. Schröder^{*,#}

[†]CellNetworks, BioQuant, Heidelberg University, Heidelberg, Germany

[‡]Institute for High-Frequency Technology, TU Braunschweig, Braunschweig, Germany

[§]Carl Zeiss NTS, Oberkochen, Germany

^{||}Karlsruhe Institute of Technology (KIT), Karlsruhe, Germany

[⊥]Multidimensional Image Processing, HCI, Heidelberg University, Heidelberg, Germany

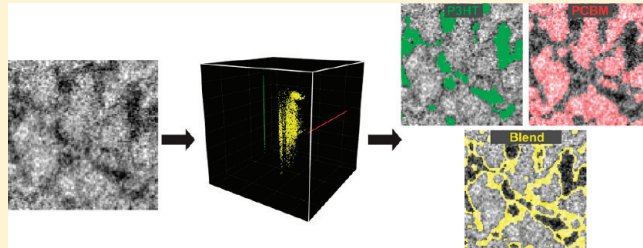
[#]InnovationLab GmbH, Heidelberg, Germany

S Supporting Information

ABSTRACT: To increase efficiency of bulk heterojunctions for photovoltaic devices, the functional morphology of active layers has to be understood, requiring visualization and discrimination of materials with very similar characteristics. Here we combine high-resolution spectroscopic imaging using an analytical transmission electron microscope with nonlinear multivariate statistical analysis for classification of multispectral image data. We obtain a visual representation showing homogeneous phases of donor and acceptor, connected by a third composite phase, depending on its extent on the way the heterojunction is fabricated.

For the first time we can correlate variations in nanoscale morphology determined by material contrast with measured solar cell efficiency. In particular we visualize a homogeneously blended phase, previously discussed to diminish charge separation in solar cell devices.

KEYWORDS: Organic photovoltaics, bulk heterojunction, transmission electron microscopy, low-energy-loss electron spectroscopic imaging, multivariate statistical analysis



Organic photovoltaic (OPV) solar cells based on polymers and small molecules are potentially superior to inorganic solar cells since they can be manufactured with little expenditure of energy on a large scale as printed, semitransparent devices on flexible substrates.^{1–4} However, efficiencies are usually very low compared to silicon-based solar cells. A solution to this problem could be provided by bulk heterojunctions (BHJs),⁵ blends of donor and acceptor materials. Here, cell efficiencies of up to 5–8% have recently been reported.^{2,6–8} An extensively studied model system is the composition of regioregular poly(3-hexylthiophene) (P3HT):methanofullerene [6,6]-phenyl C61-butyric acid methyl ester (PCBM). The manufacturing of such BHJs has been optimized for most suitable donor–acceptor interfaces: Annealing, solvent treatment, additives, or adapting materials chemical characteristics are used to establish a nanoscale interpenetrating network of donor and acceptor molecules for increasing the area for photogenerated exciton dissociation.^{9–12} To enhance the performance of such OPV, a more profound knowledge of the morphology of the photoactive organic layer is essential.

Visualizing the materials structure in BHJs is therefore crucial. Conventional imaging methods—such as atomic force microscopy¹³

as surface scanning modality, or bright field transmission electron microscopy (TEM)^{14–19}—give only limited insight into the interpenetrating network of BHJs. In TEM typical materials of photoactive layers show inherently little contrast. Image contrast arises mainly from different densities of crystalline materials,¹⁵ often enhanced by strong defocusing. Thus crystalline P3HT is visualized as elongated structures in 2D or small reconstructed volumes.^{14,20} Comparison of nonannealed and annealed films in TEM clearly reveals structural differences in images and reconstructed volumes; however, there is no proof that visible contrast corresponds to the respective materials in the heterojunction network. Even if crystal domains are visualized by bright field TEM, it remains unclear how to distinguish them from amorphous domains of P3HT and PCBM or homogeneously mixed phases, which may all be present depending on the preparation of the BHJs.^{21–23}

The crucial question is how to reliably identify these areas. Energy-filtered TEM (EFTEM) has successfully been applied to

Received: March 31, 2011

Revised: June 28, 2011

Published: July 19, 2011

create spectroscopic contrast between different materials.^{24,25} In the work presented here, we collected data using a novel generation of EFTEM with corrected spectrometer optics and monochromated beam and applied a comprehensive data correction and analysis, which allows us to separate pure and homogeneously mixed domains. We demonstrate that material contrast can be derived from spectral differences of plasmon and interband excitations. Applying multivariate statistical analysis and machine learning to the classification of multispectral images²⁶ we can identify and assign different phases to material domains on the nanoscale. We observe that spectroscopic image contrast reveals not only crystalline or homogeneous domains of P3HT and PCBM but also interconnecting mixed phases, which confirms predictions and other spectroscopic measurements.^{27–29} With our analytical TEM and data processing framework, it is now feasible to visualize spectroscopic differences with the potential to provide 3D spectroscopic contrast of multiple phases and compositions.

Samples were fabricated on ITO-coated borofloat glass with a 50 nm thick poly(3,4-ethylenedioxythiophene):poly(styrenesulfonate) (PEDOT:PSS) interlayer on top of the ITO electrode. To prepare active layers of P3HT:PCBM blends, P3HT and PCBM were dissolved in chlorobenzene in a weight ratio of 1:1 with a total concentration of 10 mg/mL for each material. For preparation of pure layers, P3HT and PCBM were dissolved in chlorobenzene individually at 10 mg/mL. The dissolved materials were spin-coated under inert atmosphere yielding thicknesses of approximately 80 and 30 nm for the blends used for electron spectroscopic imaging (ESI) and for electron-energy-loss spectroscopy (EELS), respectively. One P3HT:PCBM layer was used without annealing. One sample of P3HT:PCBM was hot plate annealed at 120 °C for 20 min. All layers used for EELS were annealed for 2 min. All of the five samples were produced in duplicate, the second set was processed further to fabricate full devices using thermally evaporated LiF layers and Al top electrodes. For electron microscopy photoactive layers were floated upon demineralized water and collected with QUANTI-FOIL holey carbon grids. EELS and ESI measurements were performed with a Libra 200 MC (Carl Zeiss NTS, Germany), providing high spatial resolution as well as high energy resolution due to the combination of a monochromator and an in-column energy filter. EEL spectra were recorded from the two pure layers P3HT and PCBM and for one BHJ annealed for 2 min. ESI stacks were recorded from the pure P3HT and PCBM samples and from two BHJ layers, one as-cast and one which was annealed for 20 min. For EELS a total electron dose of 3300 per nm² was applied, for ESI image acquisition a rate of 40000 electrons per nm² and s, the total dose was approximately 7×10^6 electrons per nm². For ESI the slit aperture was set to a width of 2 eV. Inelastic images were recorded from 2 or 3 to 30 eV in steps of 1 eV. Prior to data analysis, images were aligned by affine image registration (see Supporting Information). To classify ESI spectra, i.e., image pixels, into distinct classes, statistical analysis and machine learning were used. To this aim, we extended *ilastik*,³⁰ an open source software for image classification and segmentation. Our approach comprises two steps: In the first step—after smoothing with a narrow Gaussian filter for noise reduction (unless indicated otherwise, cf. Supporting Information)—the data dimensionality is reduced by application of local linear embedding (LLE).³¹ We found that this is superior to standard techniques like principal component analysis. LLE finds a low-dimensional representation of a nonlinear manifold—see

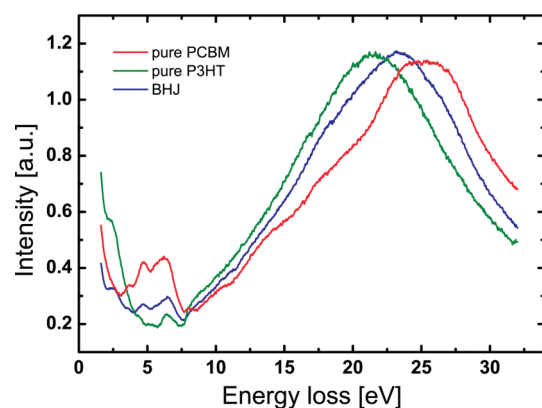


Figure 1. Normalized EEL spectra of pure films of P3HT and PCBM and a blend of weight ratio 1:1, which were annealed for 2 min at 120 °C, show different plasmon losses and fine structure around energy-losses equivalent to visible light and UV excitation energies.

Supporting Information for a detailed description. Only a subset of the available pixels is selected by manual annotation to construct the low dimensional space (bright pixels for PCBM and dark pixels for P3HT in an image where the PCBM signal is above the P3HT signal (e.g., at 28 eV)). In general, reducing the dimensionality of the data prior to training of a classifier proved to be beneficial in terms of prediction accuracy. In the second step, a Random Forest classifier³² is employed to train on the same label subsets and subsequently classify all remaining pixels/spectra. Random Forest is a supervised classifier. In the training step it builds a specified number of trees using a fixed number of randomly chosen training samples. Furthermore only a randomly chosen subset of variables (here, variables are energy loss values) are evaluated at each node to find best splitting. In the classification step all trees are used to predict the class of a spectrum, which yields maps showing P3HT and PCBM domains. The final predicted class is the one resulting from a majority voting. The algorithm offers several advantages, e.g., it is fast but due to the randomizing step it provides similar prediction accuracies as other supervised techniques.³²

EFTEM typically provides two modalities: electron-energy-loss spectroscopy (EELS) and electron spectroscopic imaging (ESI).^{33,34} Both modes were used for investigation of P3HT, PCBM, and blends of the two.

We analyzed EEL spectra to extract features that can be attributed to known electron excitations and thus to distinctive material compositions. Spectra of pure films of P3HT and PCBM and of a BHJ with a P3HT:PCBM weight ratio of 1:1 were recorded. All parameters like concentration, solvent, thickness, and annealing conditions were kept constant to exclude spectral changes due to unwanted preparative effects. The three resulting spectra are shown in Figure 1. There are two regions in the low-energy-loss range with evident features—multiple small band gap and bond excitation peaks between 2 and 8 eV and one large plasmon peak between 18 and 30 eV energy-loss. The first region contains the energies equivalent to visible to ultraviolet (UV) light. Peaks of P3HT and PCBM can be attributed to transitions known from literature^{35,36} and correspond to peaks in measurements of optical absorption spectra (Figure S1, Supporting Information). On first inspection the BHJ spectrum appears to be a linear combination of both pure spectra. We therefore performed a least-squares fit to determine the optimal coefficients for a linear combination of

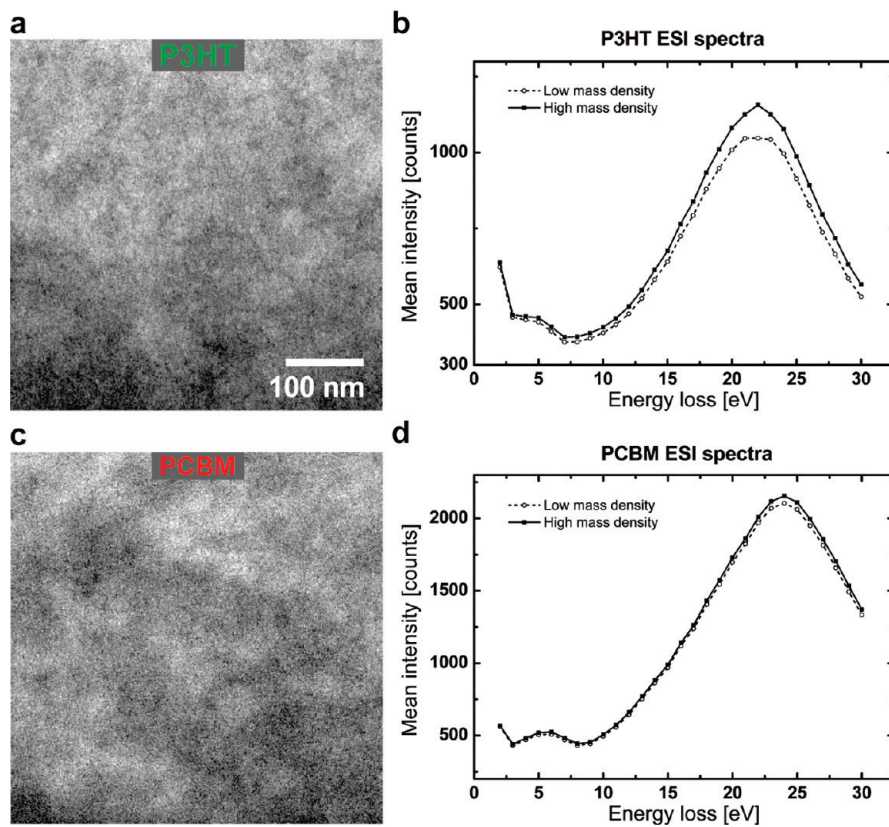


Figure 2. Zero-loss filtered images of the P3HT (a) and PCBM (c) layers provide contrast, which is mainly due to projected mass density variations. For (a) and (c) data sets were divided in two groups by applying an intensity threshold. ESI spectra for both groups were averaged. P3HT (b) and PCBM (d) spectra indeed show only intensity variations and no distinct features.

P3HT and PCBM spectra, with the constraint that the sum of both coefficients equals 1. Fitting was done for the whole spectrum and also for the plasmon peak region from approximately 10 to 32 eV alone (Figure S2, Supporting Information). The resulting modeling of the experimental spectra using the obtained fitting values illustrates that the experimental BHJ spectrum cannot be fitted without apparent residual errors. This indicates that the experimental BHJ spectrum is not solely a simple combination of spectra of the pure materials.

It should be noted that electron-energy-loss peaks of P3HT, PCBM, and the BHJ have distinct features. Thus, in general the low-loss region can be used to separate P3HT and PCBM domains by spectral imaging. In addition, as was demonstrated by Herzing et al.,²⁵ plasmon peak positions of P3HT and PCBM between 20 and 30 eV differ considerably. Plasmon peaks in Figure 1 were determined to be at \sim 21.5 and \sim 25 eV, respectively. This results in spectral energy regions around these peaks, where P3HT and PCBM produce discriminative signals. We recorded ESI spectral data sets across the entire low-loss range from about 2–3 eV up to 30 eV, in steps of 1 eV. The resulting multispectral data sets provide sampled energy-loss spectra for each image pixel. As is obvious from Figure 2a,c even in images of pure films of P3HT (Figure 2a) and PCBM (Figure 2c) zero-loss filtering produces large contrast. This contrast corresponds to projected mass density variations. To prove this, data sets were separated into two classes according to intensity. An intermediate intensity threshold was determined by Otsu segmentation and applied to the 28 eV energy-loss image leading to segmentation into regions of higher and lower mass density. The corresponding ESI spectra were averaged

yielding two average spectra that can be assigned to the two different groups of mass densities. Resulting spectra are shown in Figure 2b for P3HT and Figure 2d for PCBM. PCBM spectra of the two classes are identical except for a general increase in intensity, indicating that there is only a density variation. The differences between the two density classes of P3HT spectra vary between the very low loss and the plasmon peak energies. This may be a consequence of the thickness heterogeneities, which can lead to changes in interaction probabilities for some excitations.³⁷ Note that there are no distinct spectral shifts between spectra of the two mass density groups, indicating that image contrast in the bright field images does not represent material contrast. This is further supported by the observation that particularly the plasmon peaks of P3HT and PCBM are at significantly different energy losses.

The results of the EELS and ESI experiments on pure films indicate that this type of data collection can indeed be used to visualize specific materials. We thus applied the method to BHJ structures and compared data recorded from an as-cast blend with those from a film which was annealed at 120 °C for 20 min. In Figure 3a, a zero-loss image of the annealed BHJ is shown. This kind of image, which has been used in the past to discriminate P3HT from PCBM,¹⁴ contains similar contrast patterns as pure layers (cf. Figure 2) but no true material contrast. In contrast, inelastic images show a strong change of the observed patterns. In panels b–e of Figure 3, inelastic images from the ESI series are shown for different energy losses. The image at 3 eV appears as noisy, homogeneous intensity distribution, while the image at 6 eV reveals a similar but inverted structure to the zero-loss image

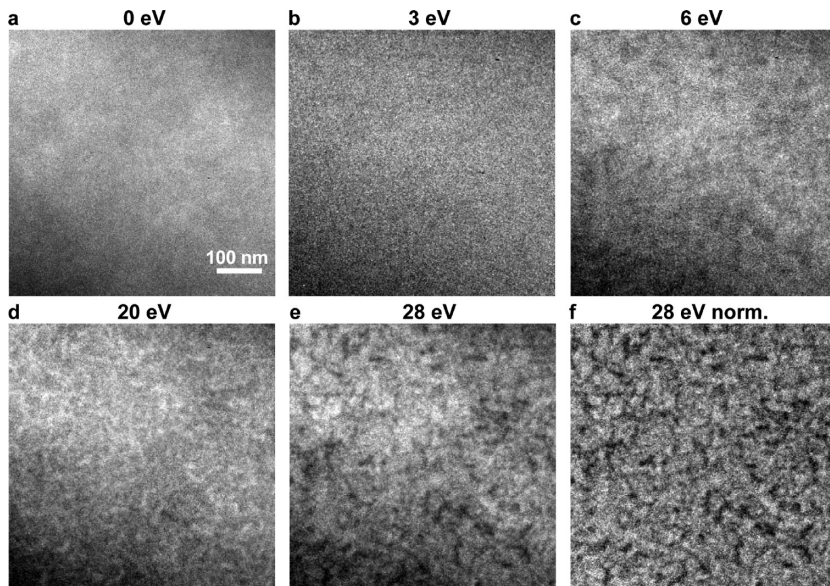


Figure 3. Low-loss images of a BHJ. (a) Zero-loss image shows only low spatial frequency contrast. (b–e) Energy-loss images from the raw ESI data stack provide varying contrasts as expected from EELS measurements. At 20 eV (d) small, elongated, bright structures are observable, which can be attributed to P3HT-rich domains because of the larger plasmon signal. This contrast is inverted in the 28 eV image (e), where former bright structures are dark and PCBM-rich domains become bright. In all images from (b–e) the underlying coarse contrast, which obstructs data analysis and classification, can still be seen. When each pixel's spectrum is normalized by its overall intensity, these variations vanish as shown in the normalized 28 eV (f) image containing only material specific domains.

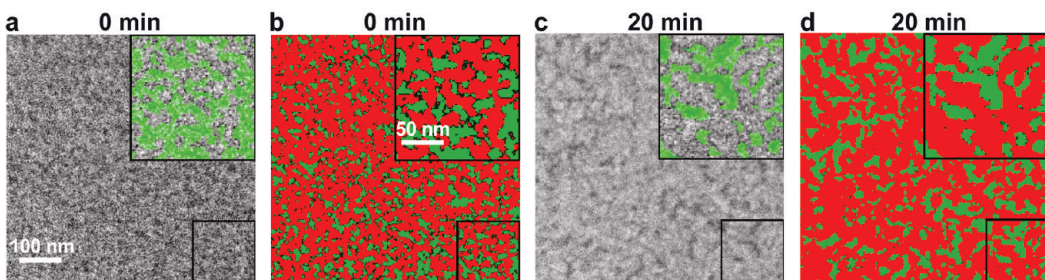


Figure 4. Images and two-class classification results of the as-cast (a, b) and annealed BHJs (c, d). Normalized energy-loss images at 28 eV (a, c) are interpreted as pure material contrast. The overlays illustrate how P3HT domains (green) are assigned to dark regions. In the classification maps of P3HT (green) and PCBM (red) in (b) and (d) different domain sizes and the more scattered distribution within the as-cast layer are visible. With two-class segmentation, PCBM domains appear to be large and strongly connected in both layers. Analysis was done with ESI stacks of images from 3 to 30 eV, in steps of 1 eV.

at 0 eV but with a subpattern of smaller features. At 20 eV small, bright, and elongated structures become visible on top of a coarse bright–dark pattern. At 28 eV these structures become dark, whereas other regions show increased intensity being similar to those in the 6 eV image. Comparing these signals to EELS signals of P3HT and PCBM implies that the inverting bright and dark regions are domains of homogeneous P3HT and PCBM. As mentioned before, the underlying low spatial frequency features are still visible. To avoid mischaracterization and misclassification of all spectra within the ESI stack, we normalized every spectrum by dividing through its integrated intensity. This removes contrast variations produced by different mass densities (cf. Figure 2). Only those characteristic features which represent a change in the shape of the spectrum remain. A representative normalized image at 28 eV (Figure 3f) shows the remaining high spatial frequency features, which are exclusively due to material contrast.

As is illustrated in Figure 3, even images at a single energy-loss provide material contrast. However, exploiting the extended spectral

information is expected to offer more discriminative power.³¹ All pixels can be categorized into specific material or material state classes. This spectral classification can be implemented using multivariate statistical analysis and machine learning.³⁸

Results of two-class separation for the as-cast layer (Figure 4a,b) are compared with those for the annealed layer (Figure 4c,d). Since at 28 eV energy loss the signal intensity of P3HT is lower than that for PCBM (cf. Figures 1 and 2) the darker regions in the inelastic image correspond to P3HT domains (Figure 4a). After the classification in two classes, the two-color map in Figure 4b is obtained, where the whole image area is classified into either P3HT or PCBM. Many small domains of P3HT are scattered within a matrix, which in this step would be assigned to PCBM. This finding would agree with the known optimal domain size of P3HT with respect to the exciton diffusion length of 5–10 nm.^{8,36} Looking at the respective map of the annealed layer (Figure 4d), larger and less scattered P3HT domains are observed within a continuous PCBM matrix. This is a

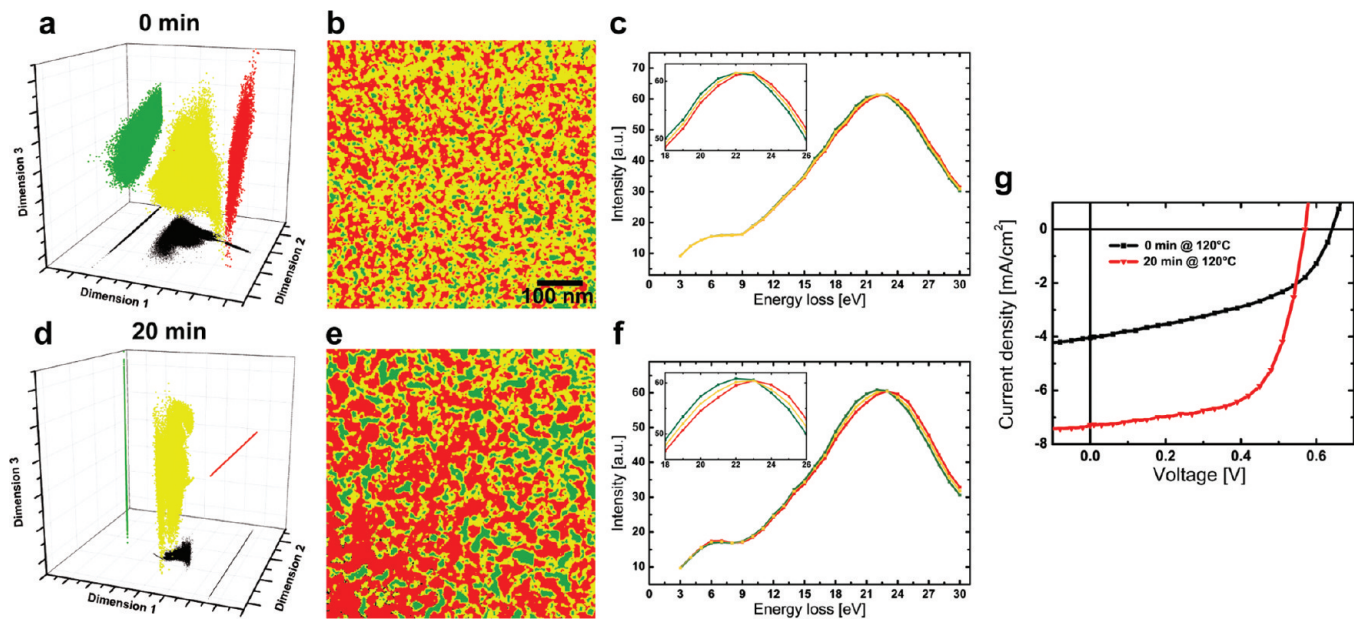


Figure 5. True domain sizes and the distribution of blend phases are obtained only after a classification of all spectra into three classes. Scatterplots (a, d) of the first three dimensions of the space spanned by LLE reveal three clusters for both the pristine (a) and the annealed (d) layers; the separation for the latter is more pronounced. After mapping class membership of all points in the scatterplots back into images (b, e) members of the yellow cluster are consistently found to create an envelope around other class areas. All regions marked in yellow are assumed to be composite regions, with a more amorphous distribution, i.e., intermixing of P3HT and PCBM. This phase is larger in the pristine layer. ESI spectra of the three classes averaged over all assigned pixels (c, f) show that indeed the three different domains correspond to different maxima of the respective plasmon energy loss. This separation is more pronounced for the annealed sample, indicating more demixing. For correlation with solar cell properties the $I-V$ curves for both samples are shown in (g).

consequence of demixing into more homogeneous domains upon annealing.³⁹

However, the novel data treatment allows further analysis of the classification process: Instead of choosing a fixed number of segmented classes, it is possible to determine the number of statistically significant classes by deriving the number of relevant data clusters in factor space. In a 3D representation of the first three vectors computed by LLE (Figure 5a,d), three clearly separated data clusters can be detected. Note that unlike the situation in principal component analysis, the separating vectors derived from LLE do not have an intuitive meaning; it is simply assumed that the first dimensions represent main variations along a nonlinear manifold. The clusters from Figure 5a,d are mapped out in Figure 5b,e. They illustrate that, as expected upon annealing, demixing into more pure and larger PCBM and P3HT domains occurs. But most interestingly, areas assigned to spectra of the third class, shown in yellow, are consistently creating a boundary between P3HT and PCBM domains. Such an arrangement and the distinct nature of the three clusters (Figure 5a,d) imply that we find a third material class, which corresponds to a blend of P3HT and PCBM. The amount of this newly visualized phase decreases upon annealing to a fraction of 0.32 of all pixels compared to the as-cast value of 0.36. An additional factor is the grade of homogeneity. In Figure 5c,f the averaged ESI spectra of the three classes are shown. Spectra of the annealed sample are significantly different, with plasmon peak positions of assigned P3HT and PCBM close to the values of EELS measurements of pure samples. The as-cast layer exhibits a by far larger degree of intermixing. This is in accordance with the assumption that demixing occurs when the layer is heated resulting in larger domains of enriched material. With increasing degree of homogeneity

of pure domains and decreasing fraction of intermediate phase, one would expect improved power conversion efficiency of a finished solar cell. The $I-V$ properties of both samples studied here are illustrated in Figure 5g. It provides characteristic values—such as short current densities, open circuit voltages and filling factors—for determination of efficiencies, which are 1.2% for as-cast and 2.6% for annealed samples. Being able to differentiate between homogeneous phases and a mixed phase, we can narrow down P3HT and PCBM domains to more truthful sizes. Davis et al. recently reported on plasmon energy-loss images to identify P3HT and PCBM domains.²⁴ However, they separated two phases by thresholding of single images. Such an approach cannot identify and localize the homogeneously mixed phase we describe here.

One possible method to assess size distribution is to analyze the power spectral density of TEM images of BHJs.¹⁶ Power spectral density plots of inelastic images at 28 eV for as-cast and annealed samples (Figure S3, Supporting Information) show onsets around 4 nm for both but a steeper rise of the signal from 14 to 65 nm for the annealed example. So features with a typical size of 14 up to 100 nm increase. Another measure to evaluate morphology is the fractal dimension of image intensity surfaces,⁴⁰ determined by box counting. It can be used to rate domain shapes. We calculated the fractal dimensions of the two P3HT maps, as 2.07 for the as-cast and 2.06 for the annealed layer. From this result we conclude that the fractal dimension is not an appropriate measure to evaluate BHJ morphology.

One concern regarding the use of nonlinear statistical analysis such as LLE is whether the occurrence of distinct clusters indeed corresponds to three independent groups of spectral signals. It could be argued that the blended phase represents a group of

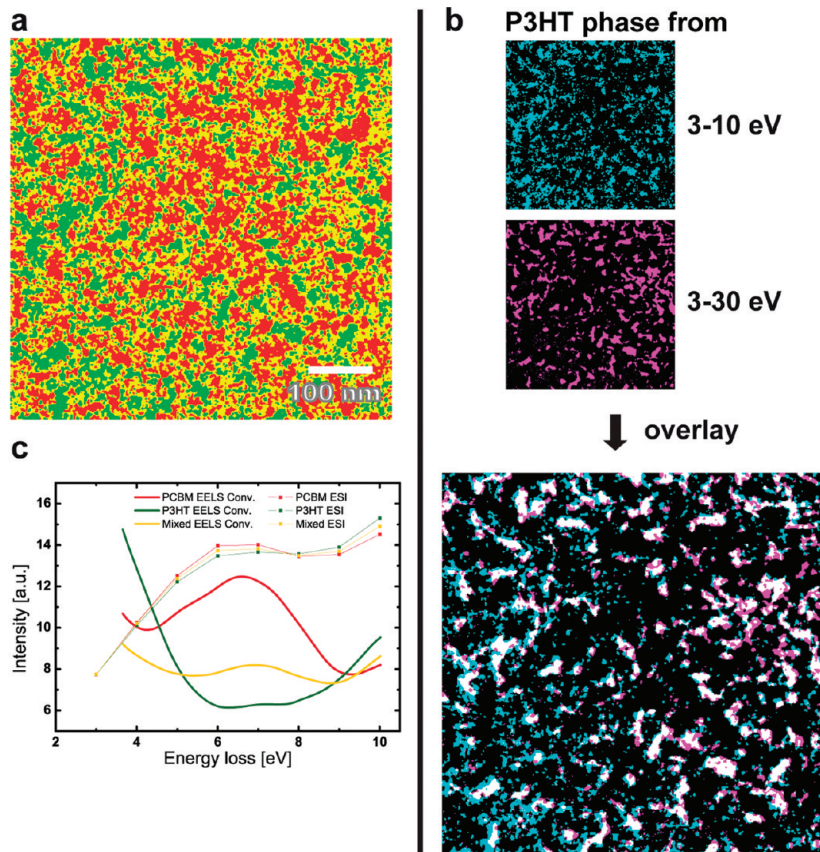


Figure 6. The annealed layer data was used to classify exactly the same area as in Figures 4 and 5, but merely with eight energy-loss images from 3 to 10 eV. Classified structures are more heterogeneous and scattered (a), showing P3HT (green), PCBM (red), and the blend (yellow) but correlate well with the result where plasmon peak signal information was included until 30 eV (cf. Figure 5). This is illustrated in the overlay (b) of both P3HT maps with the whole range classification (3–30 eV) in magenta and the low-range classification (3–10 eV) in cyan. In the overlay white pixels indicate areas where both results cross-correlate. Pixels classified into PCBM or mixed phase were omitted. ESI spectra of the three classes in (a) are averaged over all assigned pixels (c) and shown in comparison to the EEL spectra from Figure 1, which were convolved with a 2 eV box filter to simulate the effects of ESI imaging where a 2 eV broad energy-selecting slit was used.

linear combinations of P3HT and PCBM signals due to stacking of domains in the third dimension. In this case, because of multiple stacking configurations, all possible linear combinations would be observed—supposedly mimicking a third “mixing” phase. We addressed this question by performing Monte Carlo simulations. We convolved EEL spectra of P3HT and PCBM with a 2 eV mean filter, sampled in steps of 1 eV to receive pure signals comparable to ESI spectra, and computed linear combinations of these spectra. The coefficients for the combinations were sampled from a uniform distribution with varying contributions of P3HT and PCBM signals from 0 to 100%. From this we created a simulated ESI data stack. To account for the occurrence of pure domains and stacking, one part of the image contains pixels with P3HT content of 75–100%, another one with 0–25%, and a third with 25–75%. We applied statistical analysis and classification on this data set (Figure S5, Supporting Information). The three regions were identified by the classifier; however, the scatter plot of the projected data shows no distinct clouds but one continuous data cloud. In a case where the third part of the image contained only pixels of 30–70% P3HT content—i.e., combinations with 25–30% and 70–75% contents are missing—three separated clouds are observed. This finding supports our experimental data and the visualization of a distinct third material phase.

To gain insights into the actual vertical distribution without performing electron tomography, ultrathin sections of the layers perpendicular to their casting plane can be investigated. We could show that low energy-loss imaging of sections of as-cast and annealed BHJs also provides material contrast.⁴¹ For Figure S6 (Supporting Information) we applied our technique to an ultrathin section (50 nm) of a BHJ, which was annealed at 120 °C for 2 min. Although classification again reveals three phases, distinct regions in the vertical direction through the layer are observed: P3HT-rich layers are found at both interfaces (air and substrate) and a PCBM-rich layer slightly below the air interface. Only the central region contains a scattered distribution of domains. From the cross-sectional map possible charge transport paths toward interfaces can be implied.⁴¹

So far, we used the complete spectral information from 3 to 30 eV for classification. As seen with EELS (Figure 1), there is also highly discriminating functional information in the low-energy-loss window between 3 and 10 eV. Hence, we used the eight corresponding ESI images for classification. Successful discrimination by means of this reduced information would allow distinguishing other materials having similar plasmon excitations. The resulting map of the annealed sample shows three classes as illustrated in Figure 6a. Although fine structure contrast is low in the raw image (Figure 3c), structural signal appears after

normalization (Figure S7, Supporting Information). Since we limit our input data to a smaller energy window, the resulting classification is more prone to noise. However the overlay of the low loss only P3HT map with the P3HT map created from the entire information reveals that there is remarkable agreement between both (Figure 6b). Spectral differences between the three classes are compared in Figure 6c with EEL spectra. To correct for the smoothing effect of the 2 eV energy selective slit used for ESI, EEL spectra (cf. Figure 1) were convolved with a 2 eV broad box filter. This explains why differences between P3HT and PCBM are less pronounced than those observed with EELS. It should be mentioned that P3HT degrades upon irradiation due to beam damage, which leads to a change of spectral features from a typical low-dose spectrum as shown in Figure 1.

We have demonstrated that analytical transmission electron microscopy offers multiple modalities for analyzing photoactive materials. EELS can be applied to determine spectral details down to the low-energy visible light and UV range. Applying spectral imaging and multispectral data processing, we visualize different domains in BHJs. The typical resolution of this analytical imaging is determined by the delocalization of the energy-loss process which in our case is dominated by electron plasmon interactions. Such interactions are delocalized in the range of several angstroms to 1–2 nm; we therefore assume a typical structural resolution of about 1 nm for our localization maps. Material phases are found to have characteristic sizes of about 100 down to 4 nm. It is important to note that the layers studied here were comparable in thickness (\sim 80 nm). This implies that stacking of P3HT and PCBM domains in the vertical direction occurs to a certain extent. Consequently, as we project through the sample to acquire ESI images we cannot neglect the effect that this results in combinatorial spectral signals. Hence, by projection we will not identify pure domains but always obtain mixtures. This is reflected in the averaged ESI spectra of P3HT-rich and PCBM-rich domains, which exhibit stronger similarity than EEL spectra from pure layers. However, we additionally analyzed the vertical phase separation of an ultrathin cross section of an annealed BHJ, presented in this work and elsewhere.⁴¹ Classification of ESI data also yields domains of three phases but interestingly reveals that continuous layers exist near the interfaces consisting to a large extent of only P3HT or PCBM. So projecting through these layers when examining lateral distributions of floated BHJs inherently leads to linear combinations of different materials. The fact that we identify domains rich in one of the materials in lateral and vertical directions implies that these experimental results can be interpreted as signatures of enriched and mixed phases. Even though our current study is limited to the 2D projection of the OPV layers or sections, it is therefore still possible to extract valid information about the 3D interconnecting network. Of course, for quantitative, local assignments of domains in 3D, the application of electron tomography will be necessary.

Although differentiation of spectral signals is diminished by stacking, we can still identify a distinct, intermediate phase. Statistical analysis reveals three separate clusters. If the same analysis is applied to a simulated data stack containing P3HT-rich, PCBM-rich, and mixed areas of all possible linear combinations, no such separation in the projected space can be observed. This is a clear indication that the intermediate phase is indeed a distinct group of intermixed P3HT and PCBM molecules. Assuming that all observations were a consequence of stacking and, hence, inducing all kinds of linear combinations, such a clear

distinction would not be possible. Furthermore, it is conceivable that LLE as a nonlinear technique for statistical analysis identifies subtle spectral differences, which are not visible to the eye when looking at the few sampled energy-loss points of ESI spectra. We showed that the EELS signal of an annealed BHJ cannot be fully reproduced by measured pure P3HT and PCBM signals. It is possible that completely different phases—such as pure crystalline P3HT, amorphous P3HT, pure PCBM, or mixed phases of P3HT and PCBM molecules—induce slightly different spectral features apart from obvious excitation features, which is then also reflected in ESI data.

In conclusion, it is apparent that we can visualize multiple morphological conditions and spectral parameters of active layers for organic solar cells. Morphological parameters not only include domain size and connectivity but also domain purity and the extent of the described blended phase. We have proven that it is possible to use plasmon loss signals for not only structural characterization but also information from the visible light to the UV optical range. Since we applied a monochromator for high-energy resolution, it is now also possible to acquire energy-loss images down to an energy loss of 2 eV without interference of the zero-loss tail. In EEL spectra the low energy-loss region provides important fine-structure information about materials. Visualizing these differences by ESI will additionally allow the application of our technique to materials with similar plasmon excitations. However, the electron dose used to acquire the required images may also destroy the electronic structure so that the discriminative power of this region could be strongly diminished. Consequently it is strongly desired that beam stability of organic photovoltaic materials can be increased, for instance, by cooling and imaging the sample at liquid nitrogen or even liquid helium temperatures. In this case the spectrum could be sampled also at higher frequency with a smaller slit width. It will then be possible to maintain high-energy resolution in ESI.

As indicated above, the electronic structure, particularly of the polymer P3HT, is rapidly destroyed by electron beam damage. This is reflected in vanishing of Bragg reflexes in diffraction images and of low-energy-loss features in EELS signals (data not shown). At the moment this impedes the possibility of obtaining strong chemical contrast in corresponding high-resolution low-loss ESI images. Nevertheless we are certain that structural degradation at larger scale starts at much higher doses: After acquisition of the whole ESI stack, i.e., after a dose of several million electrons per nm², spatial structures in energy-loss images were still identical to structures visible at the beginning of the series.

With optimal process control of data acquisition, correction, and processing we expect that a single layer can be analyzed within 1–2 h, which will enable us to test multiple preparative effects on morphology and efficiency. By combining ESI with electron tomography to spectroscopic tomography, we further expect that we can extend this technique in order to reliably visualize morphologies of photoactive compounds in 3D.

Most importantly we found a homogeneously blended phase of P3HT and PCBM occupying the space between pure acceptor and donor domains. Its typical size decreases upon annealing, which agrees with the physical understanding of requirements to obtain efficient solar cells.^{27–29,42} As one would expect from the newly described morphological details, there are significant differences in the current–voltage properties between the as-cast and annealed devices. The as-cast device's short current density and filling factor are both low. This corresponds to the

scattered domain distribution and to the large fraction of the composite phase, a more amorphous mixture of both materials. Free charge carriers can only be transported to the electrodes at higher sheet resistance as charge separation is diminished in the homogeneously mixed phase, which is found at a larger extent in the as-cast layer. Even though the size of P3HT-rich and PCBM-rich domains increases upon annealing to values, which are larger than those for optimal exciton diffusion, annealed devices perform better. This contradiction needs to be explained: Where does the improved short current density, fill factor, and consequently the increase of efficiency from 1.2 to 2.6% result from? Many factors have to be taken into account, whose exploration necessitates multiple characterization techniques. These include diffraction methods to investigate changes in polymer packing or crystallinity. In this work, we offer a novel method to provide possible explanations by determining multiple morphological parameters to obtain structure–property relationships. Charge transport could be facilitated in the larger but purer material domains, whereas we can qualitatively evaluate the degree of enrichment by analysis of dissimilarities between spectral signals. Moreover, we found that the size of the blend phase in the annealed morphology is reduced as compared to the as-cast film; i.e., a better charge separation is achieved. Additionally it is possible to determine all illustrated morphological parameters on cross sections to identify vertical phase separation and coarse transport paths,⁴¹ which is crucial for assessing harvesting of separated charges. With optimal process control of this analytical method, we will be able to start systematic screening of organic photovoltaic cell characteristics, which will decisively enhance and accelerate the development of cells of highest efficiency.

■ ASSOCIATED CONTENT

S Supporting Information. Methodical details; discussion of low energy-loss spectral features, comparison with UV–vis absorption spectroscopy for pure layers and one BHJ; parameter fitting of the BHJ EEL spectrum as putative composite of P3HT and PCBM signals; power spectral density plots for as-cast and annealed sample; classification using nonsmoothed data; simulation of ESI data and classification; characterization of the vertical phase separation of an ultrathin section; and classification with ESI images from 3 to 10 eV. This material is available free of charge via the Internet at <http://pubs.acs.org>.

■ AUTHOR INFORMATION

Corresponding Author

*E-mail: martin.pfannmoeller@bioquant.uni-heidelberg.de

■ ACKNOWLEDGMENT

Financial support by the German Federal Ministry for Education and Research (Grant No. FKZ 13N10794-TEM), managed by the vdi, Düsseldorf, Germany, and the German National Merit Foundation (for M.P.) is gratefully acknowledged.

■ REFERENCES

- (1) Brabec, C. J.; Sariciftci, N. S.; Hummelen, J. C. *Adv. Funct. Mater.* **2001**, *11* (1), 15–26.
- (2) Dennler, G.; Scharber, M. C.; Brabec, C. J. *Adv. Mater.* **2009**, *21* (13), 1323–1338.
- (3) Schmidt, H.; Flugge, H.; Winkler, T.; Bulow, T.; Riedl, T.; Kowalsky, W. *Appl. Phys. Lett.* **2009**, *94*, 24.
- (4) Tang, C. W. *Appl. Phys. Lett.* **1986**, *48* (2), 183–185.
- (5) Halls, J. J. M.; Walsh, C. A.; Greenham, N. C.; Marseglia, E. A.; Friend, R. H.; Moratti, S. C.; Holmes, A. B. *Nature* **1995**, *376* (6540), 498–500.
- (6) Chen, H.-Y.; Hou, J.; Zhang, S.; Liang, Y.; Yang, G.; Yang, Y.; Yu, L.; Wu, Y.; Li, G. *Nat. Photonics* **2009**, *3* (11), 649–653.
- (7) Liang, Y.; Xu, Z.; Xia, J.; Tsai, S.-T.; Wu, Y.; Li, G.; Ray, C.; Yu, L. *Adv. Mater.* **2010**, *22* (20), E135–E138.
- (8) Kroese, J. E.; Savenije, T. J.; Vermeulen, M. J. W.; Warman, J. M. *J. Phys. Chem. B* **2003**, *107* (31), 7696–7705.
- (9) Flugge, H.; Schmidt, H.; Riedl, T.; Schmale, S.; Rabe, T.; Fahlbusch, J.; Danilov, M.; Speiker, H.; Schobel, J.; Kowalsky, W. *Appl. Phys. Lett.* **2010**, *97*, 12.
- (10) Hoppe, H.; Sariciftci, N. S. *J. Mater. Chem.* **2006**, *16* (1), 45–61.
- (11) Li, G.; Shrotriya, V.; Yao, Y.; Huang, J.; Yang, Y. *J. Mater. Chem.* **2007**, *17* (30), 3126–3140.
- (12) Ma, W.; Yang, C.; Gong, X.; Lee, K.; Heeger, A. J. *Adv. Funct. Mater.* **2005**, *15* (10), 1617–1622.
- (13) Spadafora, E. J.; Demadralle, R.; Ratier, B.; Grévin, B. *Nano Lett.* **2010**, *10* (9), 3337–3342.
- (14) Bavel, S. S. v.; Soury, E.; With, G. d.; Loos, J. *Nano Lett.* **2008**, *9* (2), 507–513.
- (15) Jo, J.; Kim, S.-S.; Na, S.-I.; Yu, B.-K.; Kim, D.-Y. *Adv. Funct. Mater.* **2009**, *19* (6), 866–874.
- (16) Ma, W.; Yang, C.; Heeger, A. J. *Adv. Mater.* **2007**, *19* (10), 1387–1390.
- (17) van Bavel, S. S.; Bärenklau, M.; de With, G.; Hoppe, H.; Loos, J. *Adv. Funct. Mater.* **2010**, *20* (9), 1458–1463.
- (18) Yang, X.; Loos, J.; Veenstra, S. C.; Verhees, W. J. H.; Wienk, M. M.; Kroon, J. M.; Michels, M. A. J.; Janssen, R. A. J. *Nano Lett.* **2005**, *5* (4), 579–583.
- (19) Yang, X.; Lu, G.; Li, L.; Zhou, E. *Small* **2007**, *3* (4), 611–615.
- (20) Bavel, S. S. v.; Bärenklau, M.; With, G. d.; Hoppe, H.; Loos, J. *Adv. Funct. Mater.* **2010**, *20* (9), 1458–1463.
- (21) Brinkmann, M.; Rannou, P. *Macromolecules* **2009**, *42* (4), 1125–1130.
- (22) Pingel, P.; Zen, A.; Abellón, R. D.; Grozema, F. C.; Siebbeles, L. D. A.; Neher, D. *Adv. Funct. Mater.* **2010**, *20* (14), 2286–2295.
- (23) Zen, A.; Saphiannikova, M.; Neher, D.; Grenzer, J.; Grigorian, S.; Pietsch, U.; Asawapirom, U.; Janietz, S.; Scherf, U.; Lieberwirth, I.; Wegner, G. *Macromolecules* **2006**, *39* (6), 2162–2171.
- (24) Drummy, L. F.; Davis, R. J.; Moore, D. L.; Durstock, M.; Vaia, R. A.; Hsu, J. W. P. *Chem. Mater.* **2010**, *23* (3), 907–912.
- (25) Herzing, A. A.; Richter, L. J.; Anderson, I. M. *J. Phys. Chem. C* **2010**, *114* (41), 17501–17508.
- (26) Chang, H.; Yeung, D.-Y. *Pattern Recognit.* **2006**, *39* (6), 1053–1065.
- (27) Guo, J.; Ohkita, H.; Benten, H.; Ito, S. *J. Am. Chem. Soc.* **2010**, *132* (17), 6154–6164.
- (28) Treat, N. D.; Brady, M. A.; Smith, G.; Toney, M. F.; Kramer, E. J.; Hawker, C. J.; Chabinyc, M. L. *Adv. Energy Mater.* **2011**, *1* (1), 82–89.
- (29) Tvingstedt, K.; Vandewal, K.; Zhang, F.; Inganäs, O. *J. Phys. Chem. C* **2010**, *114* (49), 21824–21832.
- (30) Sommer, C.; Straehle, C.; Köthe, U.; Hamprecht, F. A. *ilastik: Interactive Learning and Segmentation Toolkit*. In *IEEE International Symposium on Biomedical Imaging (ISBI), 8th*; IEEE: Piscataway, NJ, 2011.
- (31) Roweis, S. T.; Saul, L. K. *Science* **2000**, *290* (5500), 2323–2326.
- (32) Breiman, L. *Mach. Learn.* **2001**, *45* (1), 5–32.
- (33) Egerton, R. F. *Rep. Prog. Phys.* **2009**, *72*, 1.
- (34) Egerton, R. F.; Malac, M. J. *Electron Spectrosc. Relat. Phenom.* **2005**, *143* (2–3), 43–50.
- (35) Orlandi, G.; Negri, F. *Photochem. Photobiol. Sci.* **2002**, *1* (5), 289–308.

- (36) Theander, M.; Yartsev, A.; Zigmantas, D.; Sundström, V.; Mammo, W.; Andersson, M. R.; Inganäs, O. *Phys. Rev. B* **2000**, *61*, 19.
- (37) Reimer, L.; Kohl, H. *Transmission electron microscopy*, 5th ed.; Springer: New York, 2008.
- (38) Hanselmann, M.; Köthe, U.; Kirchner, M.; Renard, B. Y.; Amstalden, E. R.; Glunde, K.; Heeren, R. M. A.; Hamprecht, F. A. *J. Proteome Res.* **2009**, *8* (7), 3558–3567.
- (39) Zhu, X. Y.; Yang, Q.; Muntwiler, M. *Acc. Chem. Res.* **2009**, *42* (11), 1779–1787.
- (40) Gagnepain, J. J.; Roques-Carmes, C. *Wear* **1986**, *109* (1–4), 119–126.
- (41) Flügge, H.; Pfannmöller, M.; Benner, G.; Schmidt, H.; Rabe, R.; Schröder, R. R.; Kowalsky, W. *Energy Procedia*, submitted for publication, 2011.
- (42) Deibel, C.; Dyakonov, V. *Rep. Prog. Phys.* **2010**, *73* (9), 096401.